Additive Manufacturing 36 (2020) 101526

Contents lists available at ScienceDirect

Additive Manufacturing

journal homepage: www.elsevier.com/locate/addma

# Enhancing fatigue life of additive manufactured parts with electrospark deposition post-processing

Pablo D. Enrique[a,*], Ali Keshavarzkermani[a], Reza Esmaeilizadeh[a], Stephen Peterkin[b], Hamid Jahed[a], Ehsan Toyserkani[a], Norman Y. Zhou[a]

[a] University of Waterloo, 200 University Ave W, Waterloo, Ontario, N2L 3G1, Canada
[b] Huys Industries Ltd., 175 Toryork Drive, Unit 35 Weston, Ontario, M9L 1X9, Canada

ARTICLE INFO

*Keywords:*
Laser powder-bed fusion
Surface roughness
Fatigue
Electrospark deposition
Hastelloy X

ABSTRACT

Metal additive manufacturing processes allow for the production of highly dense parts with increased geometric freedom and less waste than traditional manufacturing techniques. However, one of the biggest challenges in using these parts is the relatively high surface roughness inherent to the manufacturing process. This roughness negatively affects fatigue properties and necessitates the use of post-processing surface treatments. Several methods are presented for improving local surface properties of laser powder bed fusion parts using electrospark deposition (ESD), hammer peening and heat-treatment processes. An optimized surface roughness reduction of 82% and near-surface hardness increase of 85% is obtained. Post-processed Hastelloy X parts reach $> 10^7$ cycles during fatigue testing at 350 MPa, in comparison to failure at $10^5$ cycles in the as-built condition. The improvement in mechanical properties obtained with a combined ESD and peening process shows potential for the selective enhancement of critical surface regions in additive manufactured parts.

## 1. Introduction

Additive manufacturing (AM) processes such as laser powder bed fusion (LPBF) provide significant advantages over traditional manufacturing. With reduced material waste when compared to subtractive processes and considerable geometrical freedom, LPBF is an especially attractive option for the manufacturing and lightweighting of parts made from high value materials. However, despite significant research into the subject, LPBF parts still suffer from relatively low surface quality. This has been shown to result in reduced fatigue performance, since fatigue cracks frequently initiate from surfaces at locations with higher stress concentrations [1–3]. Increased surface roughness can also negatively affect aerodynamic performance – such as in the case of turbine blades or vanes – by interacting with the boundary layer of air that flows across the surface and introducing flow instabilities [4–6].

The causes of surface roughness have been attributed to a variety of factors, including print positioning on the build plate [7], the ejection of spatter particles [8,9], the stair-step effect, and LPBF process parameters such as the printed surface orientation and thermal history [7,10,11], linear energy density, laser power, and hatch spacing [12,13]. Although process parameters can be optimized to obtain acceptable quality surfaces [14], the other contributing factors make surface quality highly variable within a single part or between parts on the same build plate. For commercial applications, some amount of post-processing that addresses surface quality is usually required.

Many surface finishing techniques are available and can be chosen based on the required final surface roughness, desired surface properties, and geometrical complexity of the part being processed. Machining is a traditional method for reducing external surface roughness [15,16], but results in material waste and is difficult to use on complex geometries. Machining is also more challenging on work hardening materials such as Ni-superalloys [17]. A reduction in surface roughness is possible via in situ layer re-melting [18] or post-process laser polishing [19] in additive manufactured parts. This technique has been demonstrated for nonplanar surfaces as well [20], although more geometrically complex parts with overhangs, lattice structures or internal channels that are not easily accessible must be addressed using other techniques.

One technique for reducing the surface roughness of internal channels – abrasive flow machining – requires a fluid with abrasive particles capable of eroding or producing micro-cuts on the part surface. Applications to additive manufactured parts have found notable reductions in surface roughness [21], although the long processing times and inconsistent material removal that depend on local shear

* Corresponding author.
*E-mail address:* pdenriqu@uwaterloo.ca (P.D. Enrique).

https://doi.org/10.1016/j.addma.2020.101526
Received 14 March 2020; Received in revised form 30 July 2020; Accepted 8 August 2020
Available online 09 August 2020

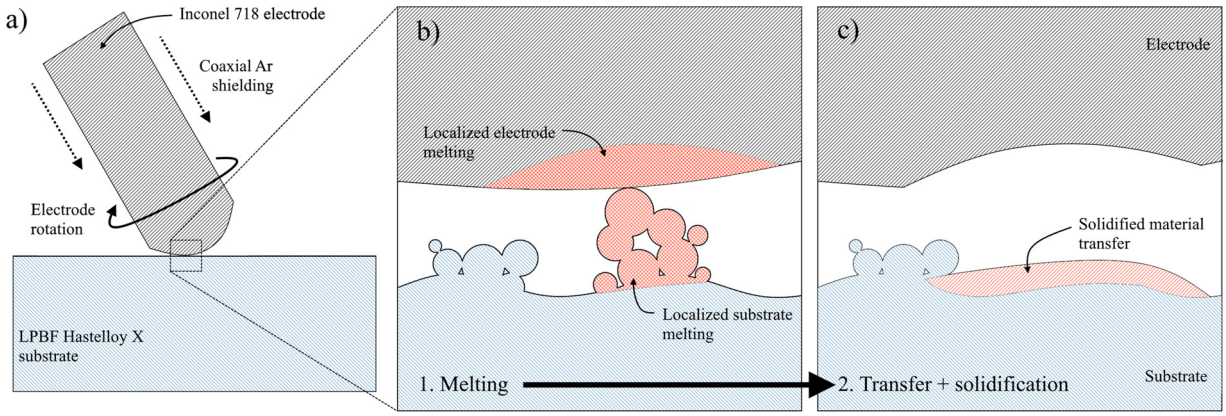


**Fig. 1.** Simplified schematic of the ESD process showing a) overview of electrode and substrate, b) localized melting of electrode and substrate during ESD, and c) material transfer and solidification.

strain rates introduce some challenges [22]. Another technique is chemical etching or electropolishing, which is shown to achieve a significant surface roughness reduction [23]. However, several disadvantages exist: this process often results in excessive material removal that can affect part tolerances [24], large features are not easily removed, the preferential dissolution of some phases in multiphase alloys can cause short range roughening [25], and conventional electropolishing methods are generally expensive, hazardous to workers, and environmentally harmful [26]. A combination of surface finishing techniques can be beneficial for applications that require a greater reduction in surface roughness and can overcome the individual disadvantages of a single process [27]. A 2-step abrasive flow machining and electrochemical machining process was successfully shown to reduce surface roughness by 80% in LPBF-made laser cutting nozzles, while improving performance over the as-built condition to match that of a conventionally manufactured part [28]. Another example identifies a 3-step process of glass blasting, vibration deburring, and dry electropolishing capable of reducing surface roughness by 93% [18].

The influence of surface finishing techniques on fatigue properties have been frequently demonstrated in literature. Chemical etching of a LPBF part resulted in a 2 times improvement in fatigue life over the as-built condition [29]. Abrasive and impact surface finishing techniques have shown similar improvements in fatigue life; the use of ultrasonic shot peening on thin struts built by electron beam melting was shown to achieve a 2 times improvement in the cycles to failure, while sandblasting was shown to improve the cycles to failure by an order of magnitude [30]. The improvements are typically attributed to a reduced surface roughness, the introduction of compressive residual stresses, or microstructural changes.

Many of these surface finishing techniques have the common characteristic of deforming or removing material from the surface. Rather than use a subtractive process, this study demonstrates the use of an additive electrospark deposition (ESD) technique and machine hammer peening to reduce surface roughness while improving the properties of external surfaces in LPBF-made Hastelloy X parts. The ESD process melts rough features on the part surface and introduces beneficial surface properties by depositing an Inconel 718 coating, while machine hammer peening flattens surface features and allows for longer ESD processing times. The combination of these two processes achieves greater surface roughness reduction with shorter processing times than the individual application of ESD or hammer peening. Several heat treatments are also investigated to address residual stresses and promote a precipitation hardening effect in the deposited Inconel 718. Although Inconel 718 and Hastelloy X are both Ni-superalloys, appropriate processing of Inconel 718 can obtain a significantly higher hardness and strength than Hastelloy X [31]. As a result of ESD and hammer peening, the surface and fatigue properties of LPBF-made Hastelloy X parts are significantly improved.

## 2. Material and methods

### 2.1. Laser powder bed fusion (LPBF)

In this study, an EOS M290 equipped with an Ytterbium fiber laser and gas atomized Hastelloy X powder with a D50 (median diameter) of 29.3 µm were used to manufacture cubic LPBF parts (10 × 15 × 30 mm). All samples were made with similar processing parameters (laser power of 200 W, laser velocity of 900 mm/s, layer thickness of 0.06 mm and hatching spacing of 0.08 mm) using a rotated stripe scanning strategy. The build plate temperature was maintained at 80 °C during the process. These samples were then post-processed for surface roughness analysis, microhardness measurements, and microstructure characterization. The same process parameters were also used to create fatigue testing samples described in Section 2.4.

### 2.2. Electrospark Deposition (ESD) and hammer peening

The side surfaces of LPBF parts were post-processed using a manually operated ESD machine and handheld machine hammer peening tool provided by Huys Industries. ESD operates by discharging a capacitor through a consumable electrode and conductive substrate. A 3.2 mm diameter Inconel 718 electrode was used as shown in Fig. 1a. During the process, small molten droplets from the electrode (Fig. 1b) are transferred to the substrate and solidified (Fig. 1c). Ultra-high purity argon shielding gas was delivered coaxially around the electrode during deposition, and ESD parameters of 100 V, 80 µF and 150 Hz were used based on previous studies that show high density and good mechanical properties [32,33]. Coatings were applied to 10 mm by 10 mm regions for various spark durations (25 s, 75 s, 125 s) in a raster scan pattern, with the pattern rotated 90° between layers. The machine hammer peening tool operates by driving a 2.5 cm long, 4.8 mm diameter hardened tool steel rod using a rotating 21 g weight offset by 0.64 mm (Fig. 2). Rotation occurs at a frequency of 100 Hz, and the vibration amplitude at the rod tip is 0.5 mm. When peening was used, the ESD process was stopped every 12.5 s and peening was applied to the entire coated area.

### 2.3. Heat treatment

Inconel 718 coated Hastelloy X samples were studied in several heat-treated conditions, described in Table 1. All heat treatments were performed in a horizontal quartz tube furnace under ultra-high purity argon gas, with a flow rate of 4 L/min and 250 Pa of positive pressure. The aging temperature and time is selected based on the industry

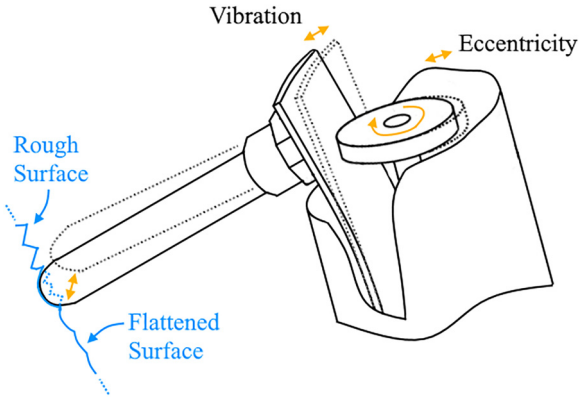


**Fig. 2.** Schematic of hammer peening tool mechanism showing vibration of a rod driven by the rotation of an eccentric weight.

**Table 1**
Heat treatments for Inconel 718 coated Hastelloy X samples.

| Sample | Heat Treatment |
|---|---|
| Direct Aged (DA) | 720 °C for 8 h, 620 °C for 10 h, air cooled |
| Solution Annealed (SA) | 1100 °C for 1 h, water quenched |
| Solution Annealed and Aged (SAA) | 1100 °C for 1 h, water quenched<br>720 °C for 8 h, 620 °C for 10 h, air cooled |

standard for Inconel 718 [34], and the solution annealing temperature and time is selected based on literature studies of secondary phase dissolution in rapid solidification processed Inconel 718 [35].

### 2.4. Characterization

Microstructure characterization was performed using a Zeiss UltraPlus scanning electron microscope (SEM) with an AMETEK EDAX Apollo XL energy-dispersive X-ray spectroscopy (EDX) attachment. A TESCAN SEM was used for the analysis of fatigue fracture surfaces, and an Oxford electron backscatter diffraction (EBSD) detector in a JEOL7000 F SEM was used for analysis of samples after heat treatment. A surface profile was obtained with a Keyence VK-X250 confocal laser microscope, and hardness results were obtained using a load of 0.1 kgf on a Wolpert Wilson 402 MVD micro Vickers hardness tester.

A combination of ESD, peening, and heat treatments were used to create several post-processed samples for surface profile analysis, microhardness evaluation, and fatigue testing. A breakdown of samples created for each analysis is provided in Table 2.

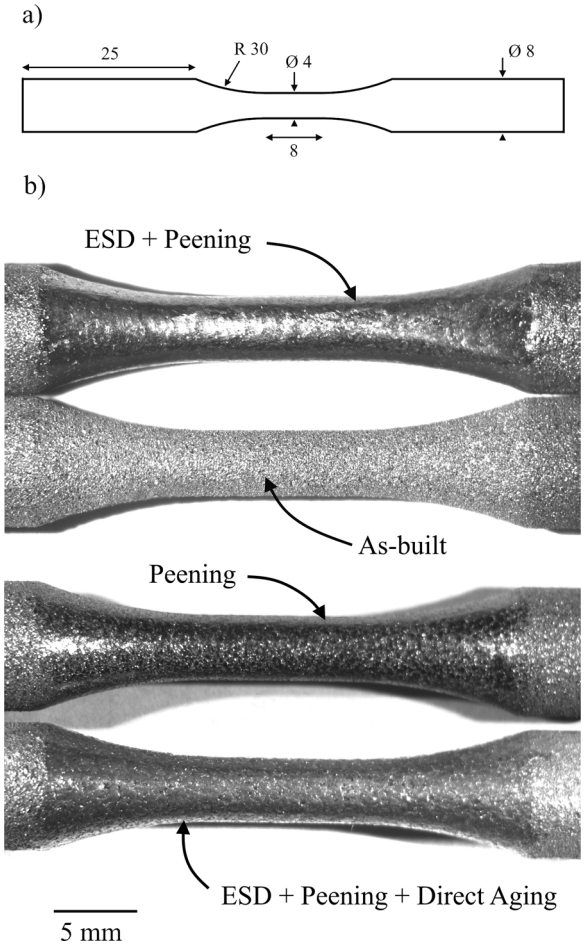


**Fig. 3.** a) Fatigue testing specimen dimensions in mm and b) samples in the as-built and post-processed conditions.

### 2.5. Fatigue testing

Post-processing of ESD + HP samples for fatigue testing consists of two layers of ESD Inconel 718 applied to the necked region of the fatigue specimens (built in a vertical orientation with dimensions shown in Fig. 3a), with peening performed at the conclusion of each layer. A second set of post-processed HP samples received an equivalent amount of peening as ESD + HP samples, without the application of an Inconel 718 coating using ESD. The last set of post-processed samples (ESD + HP + DA) were processed similarly to the ESD + HP samples, with the addition of a direct aging heat treatment. The resulting post-processed samples are compared to samples in the as-built condition,

**Table 2**
Post-processed LPBF Hastelloy X samples.

| Analysis | Sample | Sample Description |
|---|---|---|
| Surface Profile | As-built | No surface treatment |
| | ESD | With ESD Inconel 718 coating |
| | ESD + HP | With ESD Inconel 718 coating and hammer peening |
| | HP | With hammer peening |
| Microhardness | ESD | With ESD Inconel 718 coating |
| | ESD + HP | With ESD Inconel 718 coating and hammer peening |
| | ESD + HP + DA | With ESD Inconel 718 coating, hammer peening and direct aging heat treatment |
| | ESD + HP + SA | With ESD Inconel 718 coating, hammer peening and solution annealing heat treatment |
| | ESD + HP + SAA | With ESD Inconel 718 coating, hammer peening, and solution annealing + aging heat treatment |
| Fatigue life | As-built | No surface treatment |
| | HP | With hammer peening |
| | ESD + HP | With ESD Inconel 718 coating and hammer peening |
| | ESD + HP + DA | With ESD Inconel 718 coating, hammer peening and direct aging heat treatment |

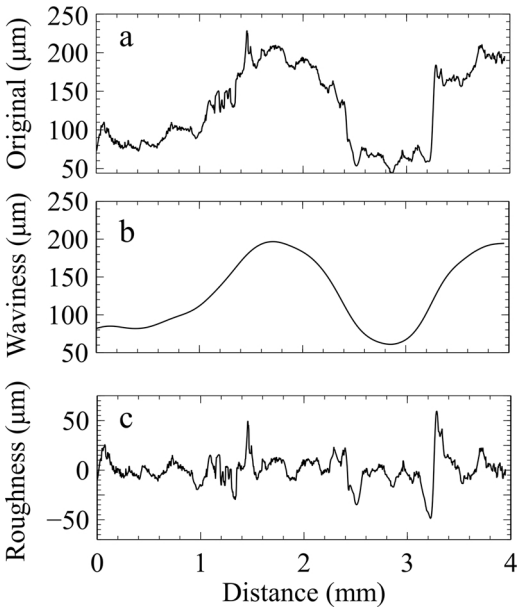


**Fig. 4.** a) Original surface profile of an as-built sample, b) long wave portion of surface profile, and c) short wave portion of surface profile.

shown in Fig. 3b.

An Instron 8872 servohydraulic fatigue testing system was used to test the room temperature fatigue performance of LPBF Hastelloy X samples with and without post-processing using a stress ratio ($R = \frac{S_{min}}{S_{max}}$) of 0.1 in tension-tension mode. Low cycle fatigue testing was performed at a maximum stress of 550 MPa while the high cycle fatigue testing was done at a maximum of 350 MPa. A frequency of 5 Hz was used for all samples except the post-processed samples tested at high cycle fatigue conditions. These samples were tested at a frequency of 5 Hz until $10^6$ cycles, and then switched to 30 Hz due to the long test durations.

### 2.6. Surface profile processing

To distinguish long-range and short-range imperfections (waviness and roughness), raw height data (Fig. 4a) was processed in MATLAB by applying a gaussian filter according to ISO 16610-21 [36]. The long wave component (Fig. 4b) was used to calculate the arithmetic mean height of the surface waviness ($W_a$), while the short wave component (Fig. 4c) was used to calculate the arithmetic mean height of the surface roughness ($S_a$).

## 3. Results and discussion

### 3.1. ESD post-processing

#### 3.1.1. Surface roughness

The most notable features on the side surface of as-built parts are the partially fused particles (PFPs) shown in Fig. 5a. The adherence of these powder particles to the side surface can be attributed to loose powder adjacent to the melt pool or spatter directed into the melt pool during the LPBF process [8]. In these conditions, partial melting of the powder in the liquid melt pool or the formation of sinter necks between the powder and the recently solidified melt pool will occur. Some roughness can also be attributed to the underlying surface, which shows distinct melt pool tracks because of the contour step performed on each layer. Since the side walls are vertical, other common contributors to surface roughness – such as the staircase effect in which angled surfaces are created using discrete steps – are not present [7].

After a short 25 s ESD time, the surface shows splash features (Fig. 5b) as a result of material transfer from the electrode. PFPs are no longer visible, likely due to re-melting of the substrate surface and coverage by material transferred from the electrode during ESD. A notable improvement to surface roughness is obtained by intermittent peening during ESD, and is clearly visible in the ESD + HP sample shown in Fig. 5c. Although deposition time is also 25 s, splash features are not visible, and the uneven surface has been mostly flattened except for some regions that were too deep to reach with the peening tool.

The etched cross-section of an ESD + HP sample part after 75 s of ESD processing time is shown in Fig. 6a. A closer look at the interface between the coating and substrate shows evidence of the Hastelloy X surface melting during ESD that removes PFPs from the surface. The cross-section in Fig. 6b shows a Hastelloy X particle – distinguishable due to its equiaxed grain structure – that has been partially melted by the ESD process. The composition profile shown in Fig. 6c identifies a 10 µm region of deposited material with lower Nb and greater Mo content than is expected from Inconel 718. Due to the spot size limitations of EDX measurements, the transition region in which Hastelloy X and Inconel 718 mix can be said to be 10 µm or less in size. Good metallurgical compatibility is expected based on the similar compositions of both materials, and the SEM/EDX analysis was unable to identify any intermetallics in the transition region.

As shown in Fig. 7a, the short deposition times (25 s) decrease the short-range surface roughness from an initial $S_a$ of 13.2 µm in the as-built samples to 6.7 µm in ESD processed samples, 6.5 µm in hammer peened (HP) samples, and 2.4 µm in ESD + HP samples (49%, 51%, and 82% decreases, respectively). The waviness also decreases from the as-built condition although to a lesser extent, from a $W_a$ of 8.8 µm to 7.2 µm in ESD samples, 6.3 µm in hammer peened (HP) samples and 4.9 µm in ESD + HP samples (18%, 28%, and 45% decreases, respectively). The surface profiles shown in Fig. 7c clearly show the effect of ESD on the surface roughness and waviness. The initial as-built surface has small localized peaks attributed to PFPs that are the major contributor to surface roughness, which are removed by the ESD process. Some longer-range waviness is present on the as-built surface and remains relatively unchanged after 25 s of ESD processing. With longer deposition times and increased material deposition these wavy features grow preferentially while the roughness remains below the as-built condition.

The ability of peening to maintain a low surface waviness in

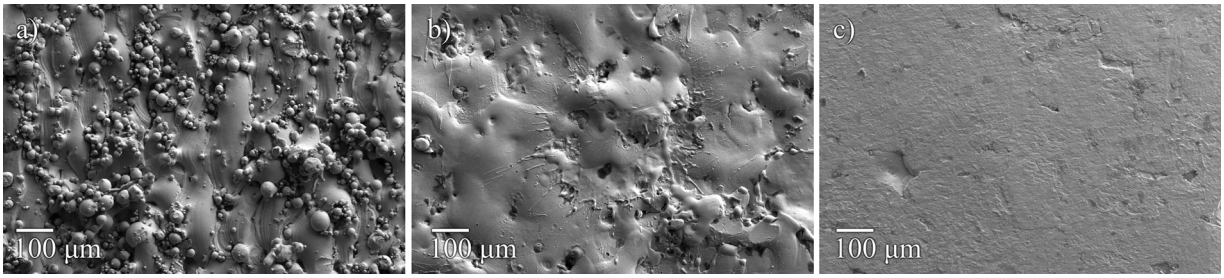


**Fig. 5.** SEM images of the side surface of an as-built LPBF Hastelloy X part a) in the as-built condition, b) after ESD coating of Inconel 718 without peening, and c) after ESD coating of Inconel 718 with peening (ESD + HP).

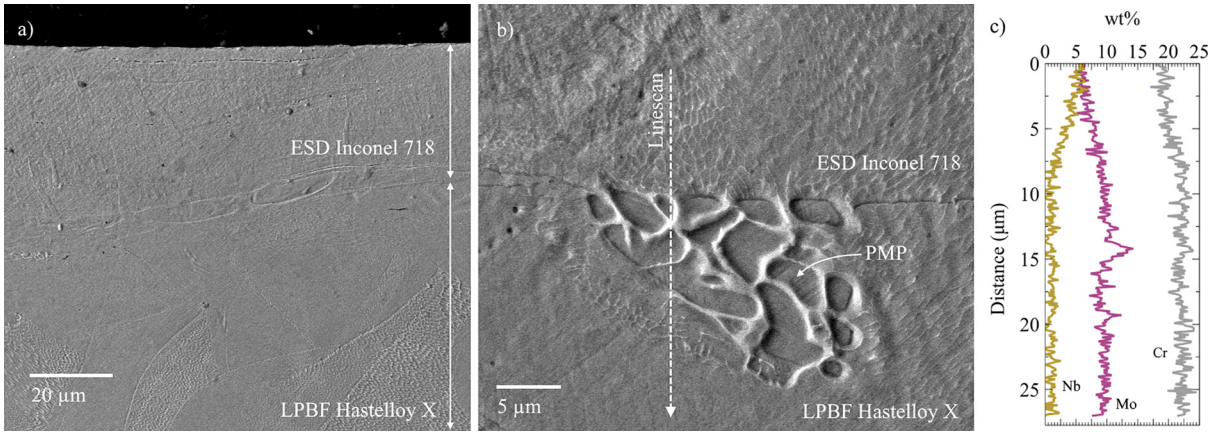


**Fig. 6.** SEM images of a) an etched ESD + HP sample cross-section, b) partially melted particle visible at the coating/substrate interface, and c) EDX line-scan as indicated in (b).

conjunction with ESD can be attributed to the mechanism by which ESD occurs. As described in [37], irregular contact geometry strongly influences where the current discharge, spark discharge, and mass transfer occurs. Current discharge occurs when the electrode and substrate make contact, which on a wavy substrate surface is at the highest protruding region. When the contact is broken, spark discharge occurs, and molten droplets are transferred from the electrode to the substrate. Due to strong electrostatic forces, material is preferentially transferred to high points on the substrate surface [37,38]. When using ESD on a LPBF-made surface, current discharge initially occurs through clusters of protruding PFPs. The sinter necks that join these PFPs to the bulk part provide for a poor connection, resulting in higher resistance to current discharge, increased joule heating and lower thermal diffusion. The result is an initial melting of these features (Fig. 5b), which reduces the surface roughness even without the use of peening (seen in Fig. 7a for short deposition times of 25 s). Further depositions produce elevated regions that further exacerbate the uneven transfer of material, forming islands as shown in Fig. 7c. However, the use of intermittent peening during ESD slows the preferential deposition on elevated regions by flattening surface irregularities that appear at shorter intervals (roughness) and preventing preferential buildup on these irregularities from forming longer interval defects (waviness). This allows longer deposition times to have more uniform coatings.

The surface melting caused by ESD is critical to achieving a low surface roughness at short processing times; a comparison to samples which were only peened (HP) in Fig. 7a shows that a combination of ESD and hammer peening is required to obtain low surface roughness, with either process being less effective when used alone. In conjunction with peening, an ESD process can be used to address both the need for reduced surface roughness and to change the surface properties of LPBF parts.

The use of peening – and by extension the surface condition of the part being coated – in ESD + HP samples has no effect on the deposition thickness (Fig. 7b), although it does have an effect on the coating distribution by minimizing the surface waviness as described previously. The similarities in deposition thickness can be seen in Fig. 7b, along

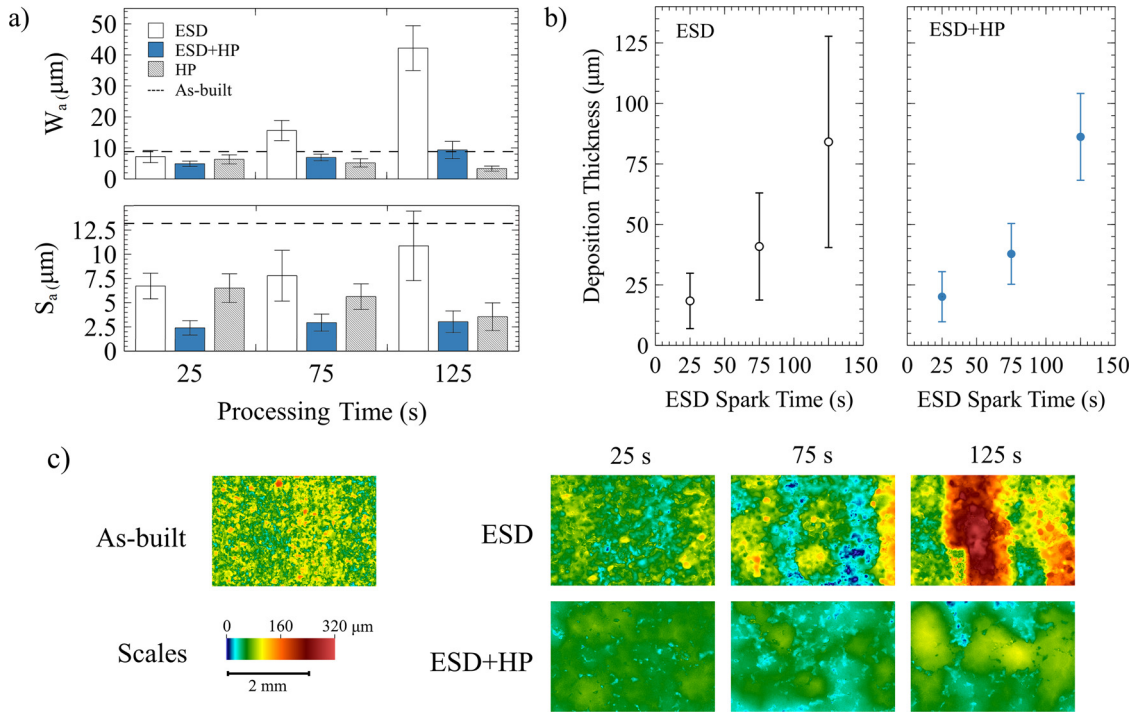


**Fig. 7.** Comparison of a) surface roughness and waviness with standard deviations, b) coating thickness with standard deviations, and c) 2D surface roughness maps for ESD coatings made using various deposition times for as-built, ESD, and ESD + HP processed samples.

**Table 3**
Levene test for average deposition thickness data in Fig. 7b comparing ESD + HP and ESD samples.

| | | ESD Spark Time | | |
|---|---|---|---|---|
| Test | Null Hypothesis (NH) | 25 s | 75 s | 125 s |
| Levene | There is no difference in the variation of the deposition thickness | $p = 0.568$ Fail to reject NH | $p < 0.001$ Reject NH | $p < 0.001$ Reject NH |

**Table 4**
Average deposition thickness ANOVA for the effect of peening and deposition time (Fig. 7b).

| | Sum of squares | df | Mean square | F | p |
|---|---|---|---|---|---|
| Peening | 3.44 | 1 | 3.44 | 1.52 | 0.218 |
| Time | 1671.4 | 2 | 835.7 | 369.78 | < .001 |
| Peening × Time | 5.49 | 2 | 2.75 | 1.22 | 0.297 |
| Residuals | 1299.5 | 575 | 2.26 | | |

with a clear difference in the standard deviation of peened (ESD + HP) and non-peened (ESD) samples. This unequal variance is quantified with the use of a Levene test [39], which shows in Table 3 a significant difference in the variance of the thicknesses between ESD + HP and ESD samples after 75 s and 125 s of ESD spark time. With the use of a Box-Cox transformation ($\lambda = 0.3$) to meet the assumptions of a normal distribution and equal variance required for an ANOVA, the effect of peening, deposition time, and their interaction could be analyzed. Only deposition time was found to influence the deposition thickness (Table 4), with p-values for peening or the interaction between the two factors above 0.05. These results, which suggest that the use of peening has no effect on the average deposition thickness but does reduce variance in the deposition thickness at longer deposition times, indicates that the quantity of material transferred during ESD is not affected by the morphology of the substrate surface. Instead, only the distribution of the transferred material changes when peening is used.

### 3.1.2. Microstructure and hardness

Inconel 718 coatings in ESD + HP samples show significantly higher hardness than LPBF Hastelloy X (471 HV vs. 283 HV), as well as the formation of a roughly 200 µm wide thermo-mechanically affected zone (TMAZ) in the Hastelloy X near the deposition interface (Fig. 8a). The effect of peening on hardness in both the deposition and TMAZ is made clear in Fig. 8b, which shows a 47 HV decrease and significant reduction of the TMAZ when peening is not used (ESD samples). However, the deposition hardness without peening (424 HV) is still high when compared to Inconel 718 in the cast (225 HV), LPBF (325 HV) or electron beam melted (355 HV) condition [40]. The difference is attributed to a faster cooling rate that forms a sub-micron cellular microstructure (Fig. 9a) and the presence of fine secondary phases (Fig. 9b) that form during deposition [41,42]. Some secondary phases are identified using EDX as oxides, ranging from sub-micron sizes to several tens of microns. As seen clearly in Fig. 9c, the oxides are rich in Al, Ti, and Nb, while also containing similar Cr and Mo content as the surrounding matrix. The following elements are arranged in terms of high to low standard free energies of formation for their oxides: Al, Ti, Nb, Cr, Fe, Mo, and Ni [43]. As such, the inclusion of Mo in the oxide is unusual and may be attributed to EDX peak overlap with Nb. The formation of these oxides is a common issue even in well-controlled high purity argon atmospheres [44,45], and may be assisted by the diffusion and segregation of elements at elevated temperatures that are favourable to oxidation [46].

The LPBF Hastelloy X substrate also exhibits a cellular subgrain microstructure (Fig. 10a) with approximately twice the primary dendrite spacing compared to the ESD processed Inconel 718 (0.8 µm vs. 0.4 µm). Oxides were also identified within as-built LPBF Hastelloy X (Fig. 10b), although with slight differences in composition compared to ESD processed Inconel 718. The oxides were determined to contain Al, Ti, and Cr, but no Mo or Nb were detected. The lack of Nb is expected since Hastelloy X does not contain Nb, while the lack of Mo can be explained by the lower oxidation potential of Mo compared to Al, Ti and Cr, as well as no opportunity for peak overlap with Nb.

### 3.2. Heat treatment of ESD post-processed parts

Three heat treatments are investigated to determine their effect on microstructure and hardness of ESD + HP samples. The first is a direct aging heat treatment that aims to precipitate the strengthening γ" phase in the deposited Inconel 718 coating. The result of this treatment on microhardness is shown in Fig. 11a. The second is an annealing heat treatment that aims to solutionize interdendritic phases, recrystalize the cellular microstructure, and remove residual stresses in the Inconel 718 coating. The result of this treatment on microhardness is shown in Fig. 11b. The third heat treatment is a combination of the prior two; a solution annealing step is performed, followed by an aging heat treatment. The result is shown in Fig. 11c.

Similar to the previously reported effect of direct aging on ESD processed Inconel 718 [33], ESD + HP + DA samples show an increased Inconel 718 hardness of 523 HV (from 471 HV) while having no significant effect on the TMAZ or Hastelloy X substrate. Aging of Inconel 718 results in the formation of carbides (Fig. 12a,b) and the formation of γ" and γ' precipitates (Fig. 12c) with $Ni_3Nb$ and $Ni_3(Al,Ti)$

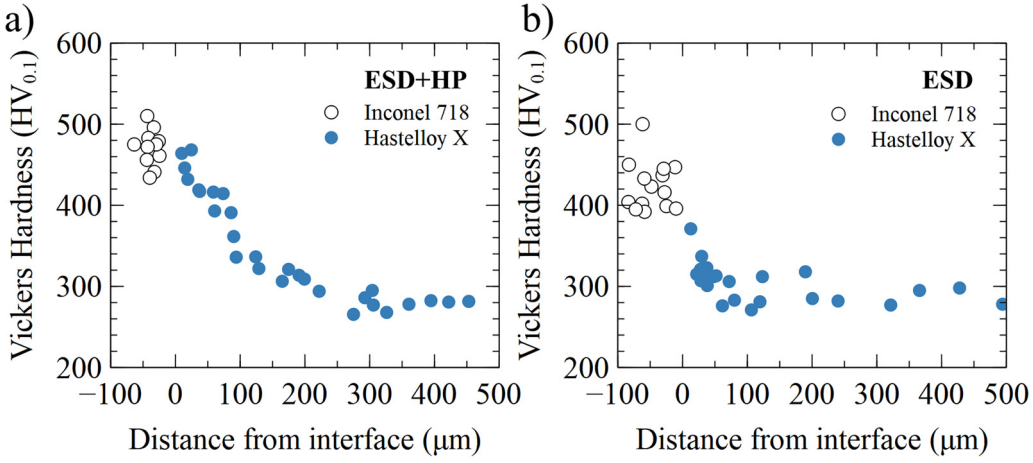


**Fig. 8.** Microhardness values for Inconel 718 coating on Hastelloy X a) with peening (ESD + HP samples) and b) without peening (ESD samples).

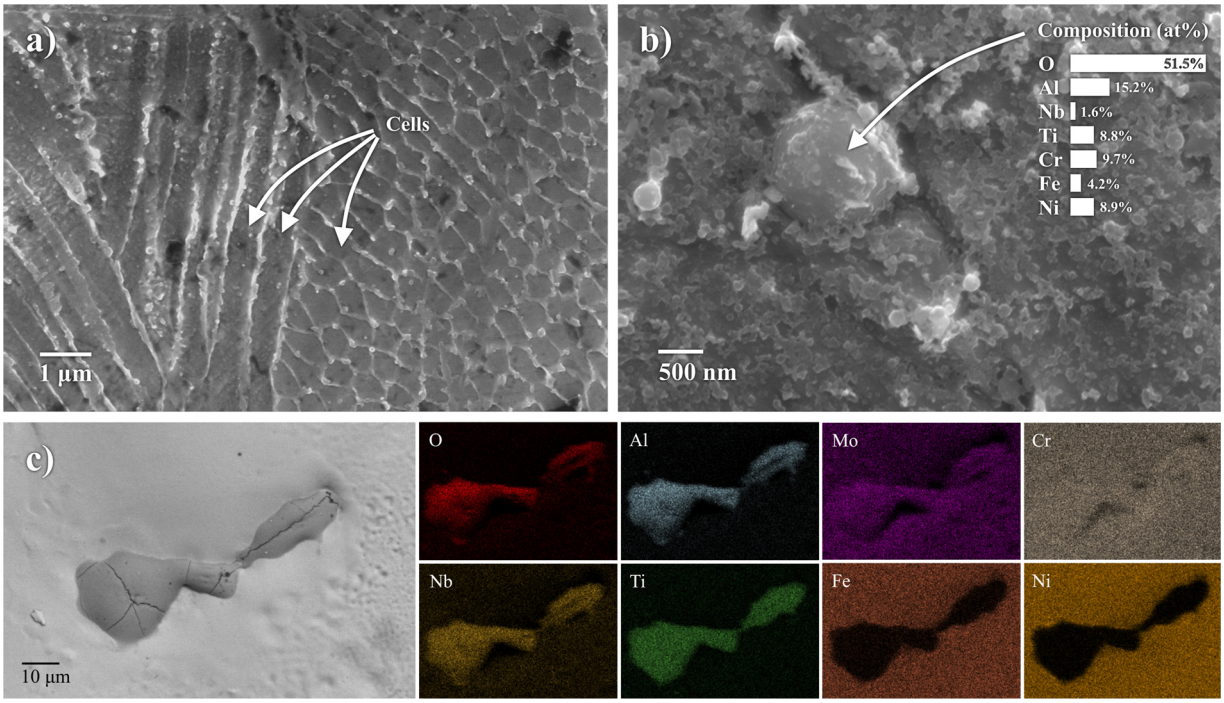


**Fig. 9.** Microstructural features found within ESD Inconel 718 coating, including a) cellular dendritic subgrains, b) small spherical oxide with EDX composition, and c) large irregularly shaped oxide with corresponding EDX composition maps.

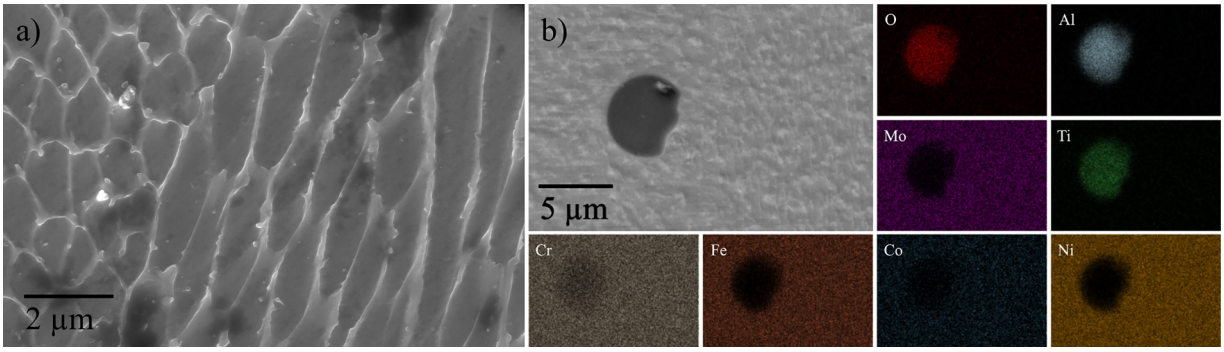


**Fig. 10.** Microstructural features found within LPBF Hastelloy X, including a) cellular subgrains and b) irregularly shaped oxide with corresponding EDX composition maps.

compositions, respectively. Since these samples are direct aged without a solutionizing step, the interdendritic eutectic and potential Laves phase that forms during solidification is retained (Fig. 12d). Without sufficient quantities of Nb, Al, or Ti in Hastelloy X, the typical γ" and γ' precipitates that contribute to an increase in strength and hardness after aging in other Ni-superalloys do not form. As such, only the deposited Inconel 718 is expected to noticeably benefit from the direct aging heat treatment.

The use of a solution annealing heat treatment in ESD + HP + SA samples reduces hardness in the deposition (from 471 HV to 390 HV) and in the TMAZ (Fig. 11b). This is attributed to the microstructural changes in the coating area after the solutionizing heat-treatment. To

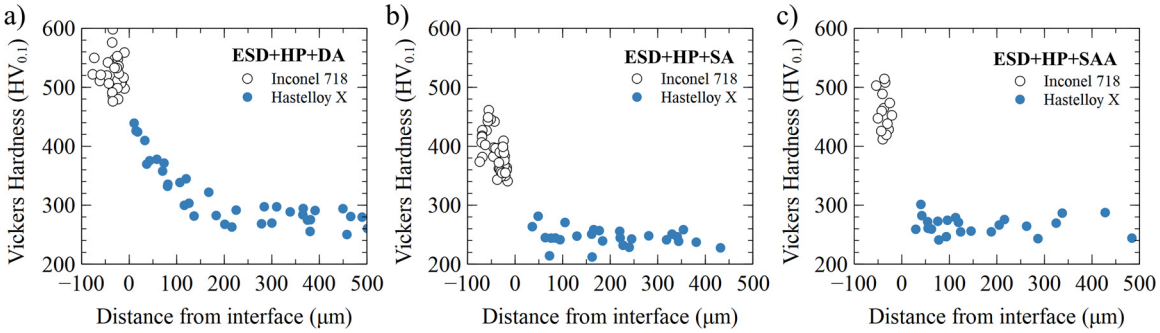


**Fig. 11.** Microhardness values for peened Inconel 718 coating on Hastelloy X after a) direct aging (ESD + HP + DA samples), b) solution annealing (ESD + HP + SA), and c) solution annealing and aging (ESD + HP + SAA).

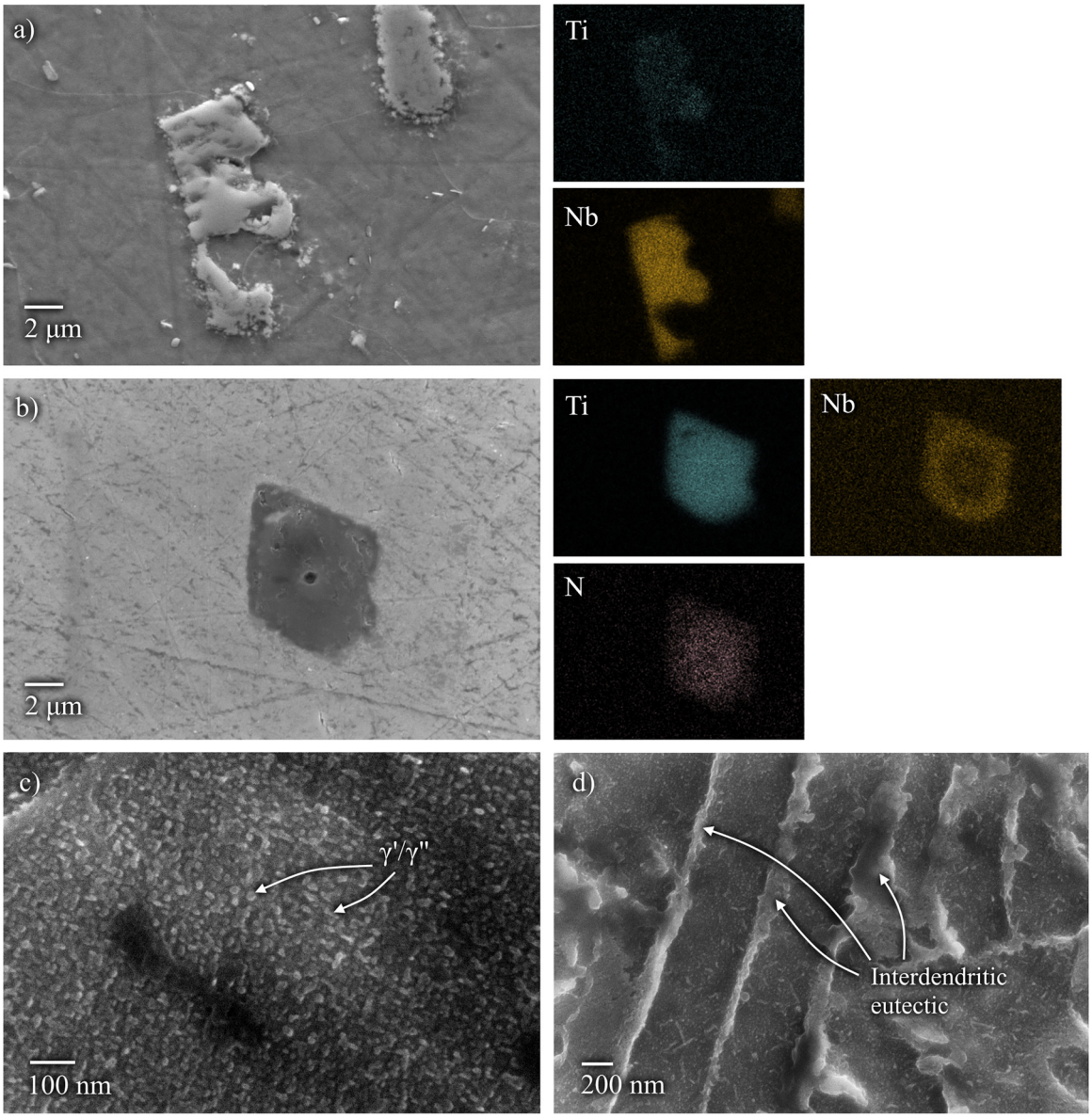


**Fig. 12.** SEM images of phases obtained after aging Inconel 718, including a) (Nb,Ti)C, b) (Ti,Nb)CN, c) γ" and γ' and d) retained interdendritic eutectic after direct aging that formed during solidification.

better characterize these changes, EBSD analysis has been performed. In the ESD + HP sample coatings, the inability to obtain clear EBSD results (Fig. 13a) is due to severe distortion in the highly deformed coating region. Literature has shown that more advanced indexing techniques are required to resolve the low quality Kikuchi patterns obtained in this region [47]. The inability to index ESD coatings also occurred in ESD sample coatings without peening, and therefore cannot be attributed solely to stresses introduced by peening. Some residual stresses can be attributed to two additional mechanisms: quenching of transferred material upon contact with a substrate that constrains its thermal contraction, and differences in coefficients of thermal expansion leading to thermal stress [48]. The very rapid cooling experienced during ESD makes the first mechanism a likely source of residual stresses, while the similar material composition between the Inconel 718 coating and Hastelloy X substrate suggests a smaller contribution from differing coefficients of thermal expansion. The resulting distorted crystal structure causes Kikuchi bands to appear diffuse [49], making EBSD analysis of grain orientation difficult. Shrinkage also affects the substrate as seen in the Kernel average misorientation (KAM) maps, which show that the local misorientation is increasing from the substrate core to the substrate/coating interface (Fig. 13b). The higher misorientation near the interface is attributed to the combination of peening and ESD, during which the first mechanism – shrinkage of the coating during cooling – and peening both apply compressive stresses on the substrate and distort the crystal structure of the grains. This results in more geometrically necessary dislocations, which corresponds to the higher hardness in the Hastelloy X substrate near the interface.

After solution annealing, the dislocation annihilation and rearrangement that occurs during recovery allows for proper indexing of the coating (Fig. 13c). A narrow misoriented region with a columnar grain morphology (Fig. 13d) is found in the coating surrounded by equiaxed ultrafine grains. This region of high misorientation is related to the pre-existing columnar grains which form due to epitaxial grain growth during rapid solidification. However, the misorientation-free regions in both the coating and TMAZ (Fig. 13d) reveals that static recrystallization occurs, with much finer recrystallized grains in the coating than in the substrate. With high dislocation density being a driving force for recrystallization, the difference in final grain size can be attributed to the higher misorientation originally present in the coating that increases the nucleation rate during recrystallization. As

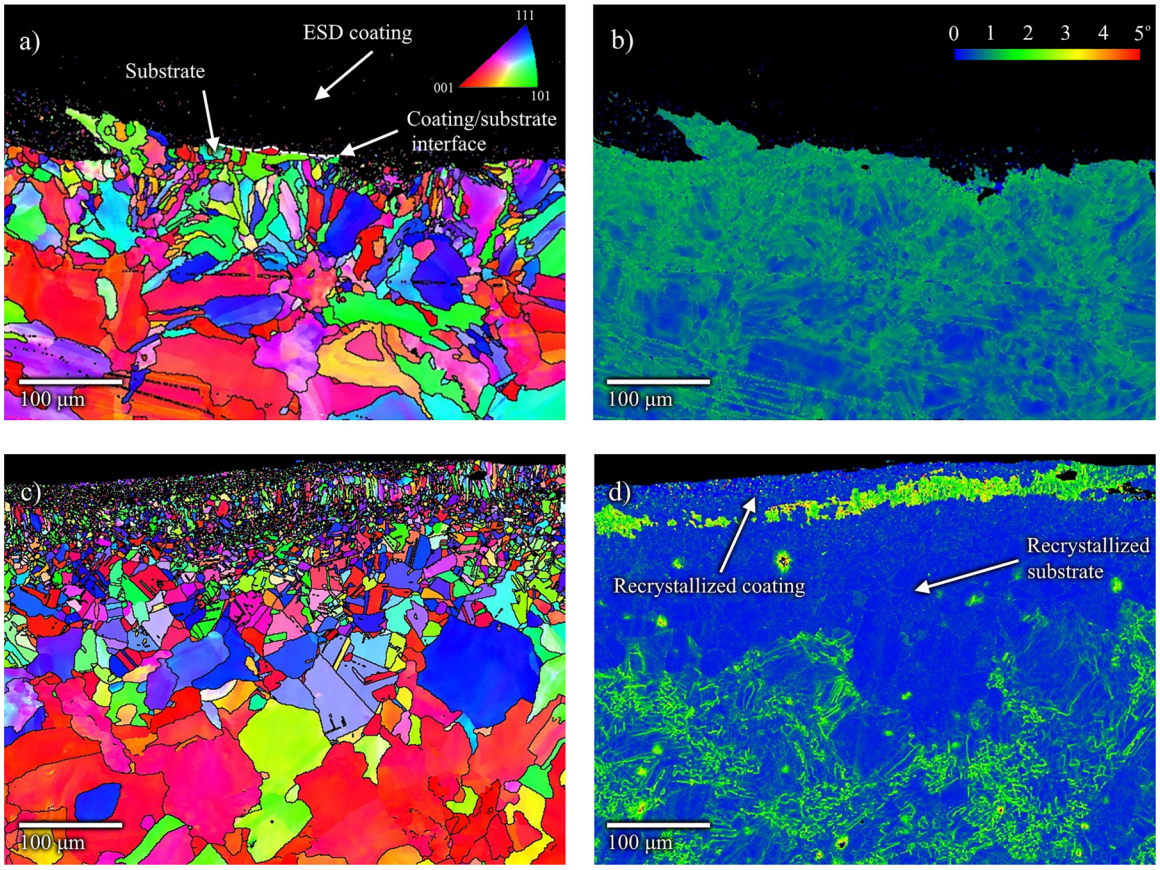


**Fig. 13.** EBSD maps for a) as-deposited coating and substrate, b) KAM map of the as-deposited sample, c) annealed and aged (ESD + HP + SAA) sample, and d) KAM map of the annealed and aged (ESD + HP + SAA) sample.

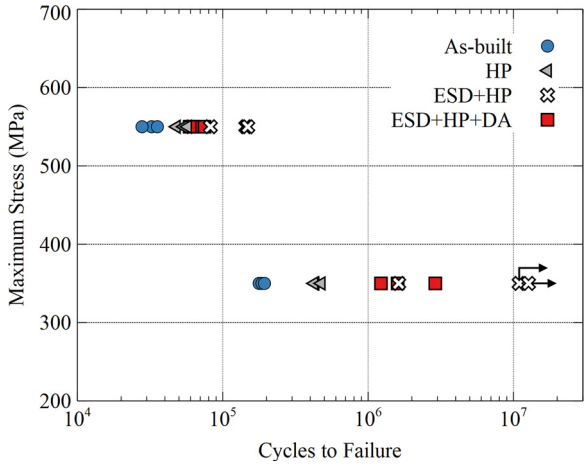


**Fig. 14.** Results of fatigue testing as-built and post-processed specimens in LCF and HCF conditions. Arrows indicate samples with interrupted tests without failures up to $10^7$ (runout).

such, even after an annealing heat treatment, the deposition hardness remains above that of cast, LPBF and EBM Inconel 718. In addition to the ultrafine grain size, some secondary phases such as oxides are not solutionized during the heat treatment and continue to contribute to the increased hardness.

At the conclusion of an aging heat treatment performed on solution annealed samples (ESD + HP + SAA), the hardness of the deposition increases to 460 HV. The 70 HV increase in the Inconel 718 hardness when comparing the annealed coating to the annealed and aged condition is attributed to the precipitation of the γ" phase. However, since residual stresses and some secondary phases have been removed during annealing, the deposition is 63 HV softer in the annealed and aged state when compared to the direct aged state.

A comparison of time-temperature-transition diagrams show that Inconel 718 is more sensitive than Hastelloy X to an aging heat treatment at 720 °C, with Inconel 718 forming the beneficial γ" phase [50]. This explains the significantly greater effect of aging on the hardness and strength of Inconel 718. Due to the lack of precipitation strengthening in Hastelloy X, the hardness outside of the TMAZ does not differ significantly after heat treatments. However, the annealing treatment may alleviate some residual stresses that occur during LPBF, which may account for the 38 HV drop between the as-built and annealed condition in Fig. 11b. Both materials also form carbide phases rapidly at 720 °C, with Hastelloy X forming $M_6C$ and $M_{23}C_6$ carbides [51]. These often have a negative influence on ductility in Hastelloy X, in addition to the negative influence on ductility from the sigma phase that forms between 650 °C and 760 °C [52].

### 3.3. Fatigue response

The room temperature low and high cycle fatigue responses (LCF and HCF, respectively) of as-built LPBF Hastelloy X are compared in Fig. 14 to post-processed specimens in the hammer peened (HP), ESD and hammer peened (ESD + HP), and ESD and hammer peened with a direct aging heat treatment (ESD + HP + DA) conditions. Two stress levels, 550 MPa for LCF and 350 MPa for HCF, were chosen for comparison, and three samples per each condition were tested at each stress level. The best performing condition (ESD + HP) showed a fatigue life improvement from 3 times to two orders of magnitude depending on the stress level. Most ESD + HP samples tested in LCF conditions showed a fatigue life improvement of up to 5 times, whereas those

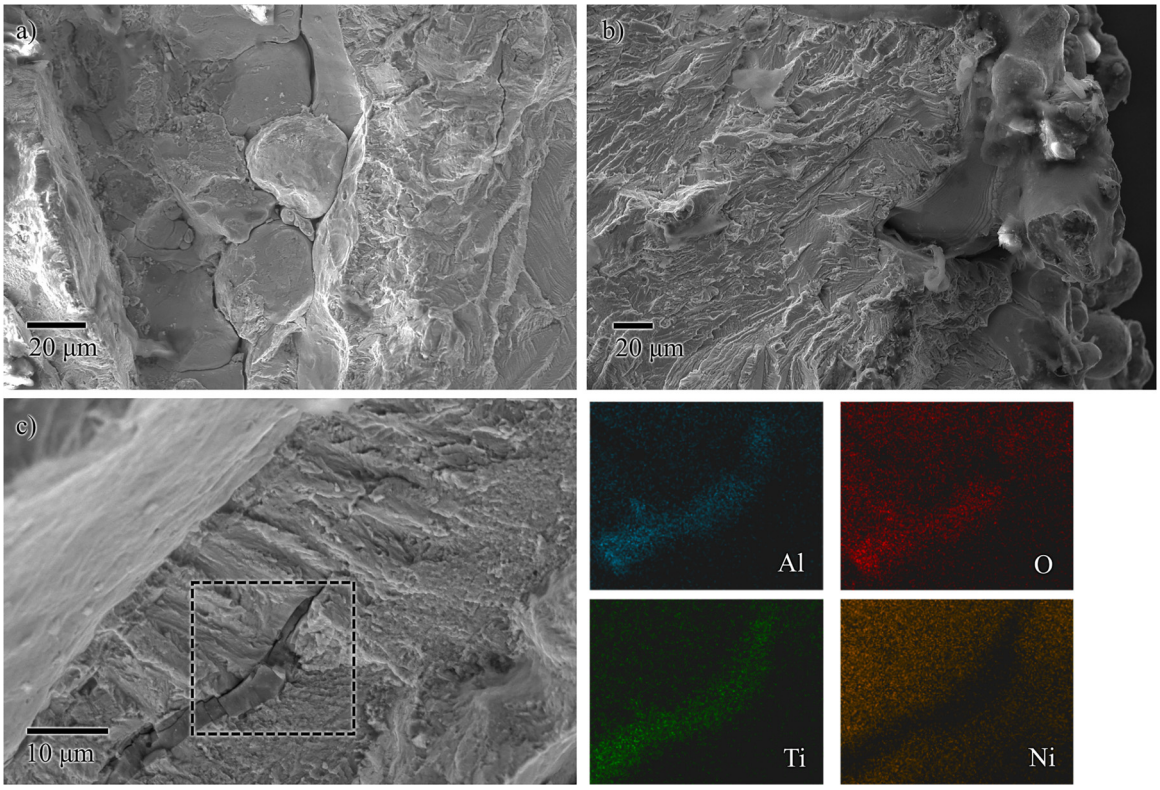


**Fig. 15.** Fracture initiation sites in a) ESD + HP sample at 350 MPa maximum stress level, b) as-built sample at 550 MPa maximum stress level, c) ESD + HP sample at 550 MPa maximum stress level with EDX map of oxide particle.

tested in HCF conditions experienced runout ($> 10^7$ cycles) for a minimum fatigue life improvement of 50 times. However, one ESD + HP sample at each test condition failed sooner, showing only 3- and 10-times improvement (for LCF and HCF, respectively) over the as-built condition. Early fatigue failure is attributed to sub-surface lack of fusion defects, while failure of the better performing samples occurred in the Inconel 718 coating due to surface defects during ESD. Further failure analysis is provided in Fig. 15. Other post-processed conditions achieved smaller improvements in fatigue life over the as-built condition. The use of hammer peening alone (HP samples) provided a 1.7- and 2.4-times improvement at LCF and HCF conditions, respectively, while the ESD + HP + DA samples showed a 2- and 10-times improvement, respectively.

Even with defects arising from LPBF and ESD, the fatigue life of samples in the ESD + HP condition are significantly improved. A comparison with the recent literature shows that the proposed ESD + HP post-processing is more effective in increasing the fatigue performance than a combined polishing (to $S_a$ of 0.33 µm) and hot isostatic pressing (HIP) technique, which could only achieve up to $9 \times 10^5$ cycles at a maximum stress of 350 MPa [53]. The significant improvement obtained by ESD + HP over the as-built or polished and HIPed condition reported in the literature can be attributed to a combination of factors including the reduction in surface roughness, the higher strength of the as-built Hastelloy X substrate and Inconel 718 coating, and residual stresses introduced as a result of hammer peening and quenching stress during ESD.

ESD parameters for the ESD + HP samples were chosen specifically to reduce the as-built surface roughness of 13.2 µm to a post-processed $S_a$ of 2.4 µm, in accordance with the results presented earlier (Fig. 7a). This reduction in surface roughness has the effect of reducing the size of notch-like features at the surface, which often act as stress risers and crack initiation sites. The influence of roughness is reflected in calculations of the endurance limit stress ($\Delta\sigma_D$), which is effectively the maximum stress below which the crack propagation of a defect does not occur. Eq. (1) is used while implementing a linear fracture mechanics approach [54]:

$$\Delta\sigma_D = \frac{\Delta K_{th}}{f K_t \sqrt{\pi a}} \tag{1}$$

where $f$ is a crack geometry dependent factor (1.122 for surface cracks), $\Delta K_{th}$ is the threshold stress intensity for crack propagation, $a$ is the crack length and $K_t$ is a stress concentration factor dependent on surface roughness. This dependence for a sample under a tensile stress state is shown in Eq. (2) [55]:

$$K_t = 1 + 2\left(\frac{S_a}{\rho}\right)\left(\frac{S_y}{S_z}\right) \tag{2}$$

where $S_a$ is the arithmetic mean height, $\rho$ is the valley profile radius, $S_y$ is the maximum absolute peak to valley height, and $S_z$ is the 10-point height. The description of $K_t$ in Eq. (2) incorporates several roughness and geometrical parameters that describe the influence of surface roughness on crack propagation from a surface notch, which is effective at predicting the fatigue life of additive manufactured parts [56]. Values of these roughness parameters for an ESD post-processed surface and original as-built surface are shown in Table 5. The use of these parameters in Eq. (2) suggests a decrease in the stress concentration factor ($K_t$) after ESD post-processing of 2.9 times, resulting in an

**Table 5**
Surface roughness parameters and stress concentration factor determined with Eq. (2).

| | As-built | ESD + HP |
|---|---|---|
| $S_a$ [µm] | 13.2 | 2.4 |
| $S_y$ [µm] | 152.48 | 90.54 |
| $S_z$ [µm] | 73.81 | 34.97 |
| $\rho$ [µm] | 8.98 | 8.63 |
| $K_t$ | 7.07 | 2.44 |

endurance limit stress 2.9 times greater than in the as-built condition according to Eq. (1).

Since a combination of ESD and hammer peening demonstrated a lower surface roughness than hammer peening alone, a greater fatigue life for ESD + HP samples when compared to HP samples is justified. This also suggests that the compressive residual stresses introduced by the peening process, which have been shown to delay crack initiation and propagation originating at the surface [57], is not likely a major contributor to the improved fatigue life. The presence of an ESD processed Inconel 718 coating in the ESD + HP samples is expected to account for some of the difference in performance. One contributor to the improved fatigue life may be attributed to the introduction of residual stresses from the quenching of deposited material during ESD. Additionally, the influence of Inconel 718′s better mechanical properties would be reflected in the value of $\Delta K_{th}$ in Eq. (1), since the threshold stress intensity factor for propagation varies depending on the material and microstructure. One benefit to ESD processed Inconel 718 is the small grain size, which has been shown to improve fatigue life by increasing boundary tortuosity and increasing the crack growth resistance in Ni-superalloys [58,59].

The lack of heat treatment in the ESD + HP condition was also found to be beneficial, since the Hastelloy X substrate and Inconel 718 coating retain both their high hardness and residual stresses introduced during peening and ESD/LPBF. High temperature heat treatments were found to be detrimental to fatigue life in literature, which caused softening of Hastelloy X [53]. However, more modest heat treatment temperatures were also found detrimental in this study. A direct aging heat treatment in ESD + HP + DA samples introduced γ” precipitates to increase strength in the Inconel 718 coating (Fig. 11a), yet still resulted in a smaller fatigue life improvement over the as-built condition when compared to ESD + HP samples (Fig. 14). Since temperatures and heat treatment times are too low to relieve residual stresses from the LPBF, ESD, or hammer peening processes (as concluded from Fig. 11a), one potential cause is the formation of detrimental grain boundary carbide or sigma phases in the Hastelloy X. These have been found to reduce room-temperature ductility in the temperature range used for direct aging in this study [52]. However, these precipitates are less brittle at elevated temperatures and were found to not influence the typical service temperature properties of Hastelloy X [52]. Although further studies are required to identify the influence of heat treatment on the microstructure and fatigue properties of LPBF-made Hastelloy X, the decrease in fatigue performance between ESD + HP and ESD + HP + DA samples indicates that the room-temperature fatigue performance is highly sensitive to Hastelloy X's heat treatment response.

Fracture surface analysis was performed on the only ESD + HP sample that failed at an HCF stress level of 350 MPa. Several sub-surface lack of fusion defects like the one shown in Fig. 15a were identified near the surface of this sample, with failure appearing to originate from these defects. The close proximity of these defects to the surface of the part is likely responsible for the premature failure, with previous studies having shown that defects nearer the surface result in a lower fatigue life [60]. An analysis of an as-built sample tested at a LCF stress level of 550 MPa shows that failure originated from roughness-related defects on the part surface, as can be seen in Fig. 15b. This also remains true of ESD + HP samples tested at 550 MPa, with Fig. 15c showing that cracking originates at the part surface. This alleviated initial concerns that brittle phases in the as-deposited Inconel 718 would encourage crack initiation and propagation [61]. A previous study identified a low fracture toughness along the interdendritic regions and droplet boundaries found in ESD processed Inconel 718 subjected to tensile testing [32]. However, the brittle interdendritic Laves phase that forms in Inconel 718 does not fracture at the low stresses investigated within this study, and has instead been shown to improve fatigue strength by hindering crack propagation [62]. Another concern is the large oxide phases identified within the Inconel 718 coating (Fig. 9c), which show cracking prior to fatigue testing and could be considered potential crack initiation sources. No evidence of this was observed, with none of the observed oxides in close proximity to the surface (Fig. 15c) acting as crack initiation sites.

## 4. Conclusions

The surface treatment of laser powder bed fusion (LPBF) made Hastelloy X samples was performed using a combined electrospark deposition (ESD) and hammer peening technique. This post-processing method addresses the surface roughness and the surface property issues of LPBF through the deposition of an Inconel 718 coating.

- A surface roughness ($R_a$) reduction of 82%, surface hardness increase of 85%, and Inconel 718 coating of 20 μm was obtained with an ESD spark time of 25 s in a 1 $cm^2$ area and hammer peening. Although peening reduced surface roughness, increased the hardness of the deposited coating, and increased the size of the thermo-mechanically affected zone (TMAZ), it was not found to influence the average coating thickness.
- The use of typical Inconel 718 heat treatments had limited effect on the LPBF additive manufactured Hastelloy X substrate hardness while significantly altering the microstructure and hardness of the Inconel 718 coating. Direct aged samples showed an increase in hardness alongside a precipitation of the γ” and γ’ phases. An annealing and aging heat treatment partially recrystallized the Inconel 718 grain structure and eliminated the TMAZ prior to forming the strengthening γ” and γ’ phases.
- The use of an ESD Inconel 718 coating and hammer peening on LPBF additive manufactured Hastelloy X resulted in a greater than 50 times improvement in fatigue life (reaching $> 10^7$cycles) at a stress of 350 MPa and an up to 5 times improvement in fatigue life (to $1.5 \times 10^5$ cycles) at a stress of 550 MPa. The improvement in the endurance limit can be primarily attributed to a reduction in surface roughness and better properties of the coating material.

## CRediT authorship contribution statement

**Pablo D. Enrique:** Writing - original draft, Conceptualization, Formal analysis, Investigation, Visualization, Project administration. **Ali Keshavarzkermani:** Writing - review & editing, Conceptualization, Investigation. **Reza Esmaeilizadeh:** Writing - review & editing, Conceptualization, Investigation. **Stephen Peterkin:** Writing - review & editing, Resources, Investigation. **Hamid Jahed:** Writing - review & editing, Resources, Supervision. **Ehsan Toyserkani:** Writing - review & editing, Resources, Supervision. **Norman Y. Zhou:** Writing - review & editing, Resources, Supervision, Funding acquisition.

## Declaration of Competing Interest

The authors declare that they have no known competing financial interests or personal relationships that could have appeared to influence the work reported in this paper.

## Acknowledgements

This work was performed with funding support from the Natural Sciences and Engineering Research Council of Canada (NSERC), the Canada Research Chairs (CRC) Program, Huys Industries, the CWB Welding Foundation and the Federal Economic Development Agency for Southern Ontario (FedDev Ontario), in collaboration with the Centre for Advanced Materials Joining, the Multi-Scale Additive Manufacturing Lab, and the Fatigue and Stress Analysis Lab at the University of Waterloo.

## References


[1] S. Afkhami, M. Dabiri, S.H. Alavi, T. Björk, A. Salminen, Fatigue characteristics of steels manufactured by selective laser melting, Int. J. Fatigue 122 (2019) 72–83, https://doi.org/10.1016/j.ijfatigue.2018.12.029.

[2] G. Kasperovich, J. Hausmann, Improvement of fatigue resistance and ductility of TiAl6V4 processed by selective laser melting, J. Mater. Process. Technol. 220 (2015) 202–214, https://doi.org/10.1016/j.jmatprotec.2015.01.025.

[3] S. Bagehorn, J. Wehr, H.J. Maier, Application of mechanical surface finishing processes for roughness reduction and fatigue improvement of additively manufactured Ti-6Al-4V parts, Int. J. Fatigue 102 (2017) 135–142, https://doi.org/10.1016/j.ijfatigue.2017.05.008.

[4] K. Bammert, H. Sandstede, Measurements of the boundary layer development along a turbine blade with rough surfaces, Am. Soc. Mech. Eng. 102 (1980) 978–983.

[5] Y. Il Yun, I.Y. Park, S.J. Song, Performance degradation due to blade surface roughness in a single-stage axial turbine, J. Turbomach. 127 (2005) 137–143, https://doi.org/10.1115/1.1811097.

[6] Q. Zhang, P.M. Ligrani, Aerodynamic losses of a cambered turbine vane: influences of surface roughness and freestream turbulence intensity, J. Turbomach. 128 (2006) 536–546, https://doi.org/10.1115/1.2185125.

[7] Z. Chen, X. Wu, D. Tomus, C.H.J. Davies, Surface roughness of selective laser melted Ti-6Al-4V alloy components, Addit. Manuf. 21 (2018) 91–103, https://doi.org/10.1016/j.addma.2018.02.009.

[8] U. Ali, R. Esmaeilizadeh, F. Ahmed, D. Sarker, W. Muhammad, A. Keshavarzkermani, Y. Mahmoodkhani, E. Marzbanrad, E. Toyserkani, Identification and characterization of spatter particles and their effect on surface roughness, density and mechanical response of 17-4 PH stainless steel laser powder-bed fusion parts, Mater. Sci. Eng. A 756 (2019) 98–107, https://doi.org/10.1016/j.msea.2019.04.026.

[9] R. Esmaeilizadeh, U. Ali, A. Keshavarzkermani, Y. Mahmoodkhani, E. Marzbanrad, E. Toyserkani, On the effect of spatter particles distribution on the quality of Hastelloy X parts made by laser powder-bed fusion additive manufacturing, J. Manuf. Process. 37 (2019) 11–20, https://doi.org/10.1016/j.jmapro.2018.11.012.

[10] Z. Dong, Y. Liu, W. Li, J. Liang, Orientation dependency for microstructure, geometric accuracy and mechanical properties of selective laser melting AlSi10Mg lattices, J. Alloys Compd. 791 (2019) 490–500, https://doi.org/10.1016/j.jallcom.2019.03.344.

[11] F. Calignano, Investigation of the accuracy and roughness in the laser powder bed fusion process, Virtual Phys. Prototyp. 13 (2018) 97–104, https://doi.org/10.1080/17452759.2018.1426368.

[12] T. Yang, T. Liu, W. Liao, E. MacDonald, H. Wei, X. Chen, L. Jiang, The influence of process parameters on vertical surface roughness of the AlSi10Mg parts fabricated by selective laser melting, J. Mater. Process. Technol. 266 (2019) 26–36, https://doi.org/10.1016/j.jmatprotec.2018.10.015.

[13] R. Mertens, S. Clijsters, K. Kempen, J.-P. Kruth, Optimization of scan strategies in selective laser melting of aluminum parts with downfacing areas, J. Manuf. Sci. Eng. 136 (2014) 061012, , https://doi.org/10.1115/1.4028620.

[14] S. Patel, A. Rogalsky, M. Vlasea, Towards understanding side-skin surface characteristics in laser powder bed fusion, J. Mater. Res. (2020), https://doi.org/10.1557/jmr.2020.125.

[15] O. Oyelola, P. Crawforth, R. M'Saoubi, A.T. Clare, Machining of additively manufactured parts: implications for surface integrity, Procedia CIRP 45 (2016) 119–122, https://doi.org/10.1016/j.procir.2016.02.066.

[16] G. Rotella, S. Imbrogno, S. Candamano, D. Umbrello, Surface integrity of machined additively manufactured Ti alloys, J. Mater. Process. Technol. 259 (2018) 180–185, https://doi.org/10.1016/j.jmatprotec.2018.04.030.

[17] I.A. Choudhury, M.A. El-Baradie, Machinability of nickel-base super alloys: a general review, J. Mater. Process. Technol. 300 (1998) 278–284, https://doi.org/10.1016/s0924-0136(97)00429-9.

[18] D. Loaldi, M. Kain, G. Tosello, Comparison of selective laser melting Post-processes based on amplitude and functional surface roughness parameters, Jt. Spec. Interes. Gr. Meet. Between Euspen ASPE Adv. Precis. Addit. Manuf. (2019).

[19] A. Lamikiz, J.A. Sánchez, L.N. López de Lacalle, J.L. Arana, Laser polishing of parts built up by selective laser sintering, Int. J. Mach. Tools Manuf. 47 (2007) 2040–2050, https://doi.org/10.1016/j.ijmachtools.2007.01.013.

[20] K.C. Yung, T.Y. Xiao, H.S. Choy, W.J. Wang, Z.X. Cai, Laser polishing of additive manufactured CoCr alloy components with complex surface geometry, J. Mater. Process. Technol. 262 (2018) 53–64, https://doi.org/10.1016/j.jmatprotec.2018.06.019.

[21] X. Wang, S. Li, Y. Fu, H. Gao, Finishing of additively manufactured metal parts by abrasive flow machining, Solid Free. Fabr. 2016 Proc. 27th Annu. Int. Solid Free. Fabr. Symp. - An Addit. Manuf. Conf. SFF 2016, 2016, pp. 2470–2472.

[22] E. Uhlmann, C. Schmiedel, J. Wendler, CFD simulation of the abrasive flow machining process, Procedia CIRP 31 (2015) 209–214, https://doi.org/10.1016/j.procir.2015.03.091.

[23] S. Sarkar, C.S. Kumar, A.K. Nath, Effects of different surface modifications on the fatigue life of selective laser melted 15–5 PH stainless steel, Mater. Sci. Eng. A. 762 (2019) 138109, https://doi.org/10.1016/j.msea.2019.138109.

[24] V. Urlea, V. Brailovski, Electropolishing and electropolishing-related allowances for powder bed selectively laser-melted Ti-6Al-4V alloy components, J. Mater. Process. Technol. 242 (2017) 1–11, https://doi.org/10.1016/j.jmatprotec.2016.11.014.

[25] D. Zhu, L. Yu, R. Zhang, Dissolution effects with different microstructures of inconel 718 on surface integrity in electrochemical machining, J. Electrochem. Soc. 165 (2018) E872–E878, https://doi.org/10.1149/2.0761816jes.

[26] E.J. Taylor, M. Inman, Electrochemical surface finishing, Electrochem. Soc. Interface 23 (2014) 57–61, https://doi.org/10.1149/2.F05143if.

[27] V. Finazzi, A.G. Demir, C.A. Biffi, F. Migliavacca, L. Petrini, B. Previtali, Design and functional testing of a novel balloon-expandable cardiovascular stent in CoCr alloy produced by selective laser melting, J. Manuf. Process. 55 (2020) 161–173, https://doi.org/10.1016/j.jmapro.2020.03.060.

[28] M. Anilli, A.G. Demir, B. Previtali, Additive manufacturing of laser cutting nozzles by SLM: processing, finishing and functional characterization, Rapid Prototyp. J. 24 (2018) 562–583, https://doi.org/10.1108/RPJ-05-2017-0106.

[29] A. Cutolo, B. Neirinck, K. Lietaert, C. de Formanoir, B. Van Hooreweder, Influence of layer thickness and post-process treatments on the fatigue properties of CoCr scaffolds produced by laser powder bed fusion, Addit. Manuf. 23 (2018) 498–504, https://doi.org/10.1016/j.addma.2018.07.008.

[30] L. Denti, A. Sola, On the effectiveness of different surface finishing techniques on A357.0 parts produced by laser-based powder bed fusion: surface roughness and fatigue strength, Metals (Basel). 9 (2019) 1284, https://doi.org/10.3390/met9121284.

[31] M.J. Donachie, S.J. Donachie, Superalloys: A Technical Guide, ASM International, 2002, https://doi.org/10.1361/stgs2002p001.

[32] P.D. Enrique, Z. Jiao, N.Y. Zhou, E. Toyserkani, Effect of microstructure on tensile properties of electrospark deposition repaired Ni-superalloy, Mater. Sci. Eng. A. 729 (2018) 268–275, https://doi.org/10.1016/j.msea.2018.05.049.

[33] P.D. Enrique, Z. Jiao, N.Y. Zhou, Effect of direct aging on heat-affected zone and tensile properties of electrospark-deposited alloy 718, Metall. Mater. Trans. A. 50 (2019) 285–294, https://doi.org/10.1007/s11661-018-4997-1.

[34] J.R. Davis, ASM Specialty Handbook: Heat-Resistant Materials, ASM International, 1997.

[35] S. Sui, C. Zhong, J. Chen, A. Gasser, W. Huang, J.H. Schleifenbaum, Influence of solution heat treatment on microstructure and tensile properties of Inconel 718 formed by high-deposition-rate laser metal deposition, J. Alloys. Compd. 740 (2018) 389–399, https://doi.org/10.1016/j.jallcom.2017.11.004.

[36] J. Vit, Surface Metrology Open Profile Gaussian Filter, (2015) https://www.mathworks.com/matlabcentral/fileexchange/52892-surface-metrology-open-profile-gaussian-filter.

[37] S. Frangini, A. Masci, A study on the effect of a dynamic contact force control for improving electrospark coating properties, Surf. Coatings Technol. 204 (2010) 2613–2623, https://doi.org/10.1016/j.surfcoat.2010.02.006.

[38] A.V. Ribalko, K. Korkmaz, O. Sahin, Intensification of the anodic erosion in electrospark alloying by the employment of pulse group, Surf. Coatings Technol. 202 (2008) 3591–3599, https://doi.org/10.1016/j.surfcoat.2007.12.037.

[39] K.F. Weaver, V.C. Morales, S.L. Dunn, K. Godde, P.F. Weaver, An Introduction to Statistical Analysis in Research: With Applications in the Biological and Life Sciences, (2017), https://doi.org/10.1002/9781119454205.

[40] E. Hosseini, V.A. Popovich, A review of mechanical properties of additively manufactured Inconel 718, Addit. Manuf. 30 (2019) 100877, https://doi.org/10.1016/j.addma.2019.100877.

[41] E. Anisimov, A.K. Khan, O.A. Ojo, Analysis of microstructure in electro-spark deposited IN718 superalloy, Mater. Charact. 119 (2016) 233–240, https://doi.org/10.1016/j.matchar.2016.07.025.

[42] P.D. Enrique, Z. Jiao, N.Y. Zhou, E. Toyserkani, Dendritic coarsening model for rapid solidification of Ni-superalloy via electrospark deposition, J. Mater. Process. Technol. 258 (2018) 138–143, https://doi.org/10.1016/j.jmatprotec.2018.03.023.

[43] T.B. Reed, Free Energy of Formation of Binary Compounds: An Atlas of Charts for High-temperature Chemical Calculations, MIT Press, 1971.

[44] A.N.D. Gasper, B. Szost, X. Wang, D. Johns, S. Sharma, A.T. Clare, I.A. Ashcroft, Spatter and oxide formation in laser powder bed fusion of Inconel 718, Addit. Manuf. 24 (2018) 446–456, https://doi.org/10.1016/j.addma.2018.09.032.

[45] Y.N. Zhang, X. Cao, P. Wanjara, M. Medraj, Oxide films in laser additive manufactured Inconel 718, Acta Mater. 61 (2013) 6562–6576, https://doi.org/10.1016/j.actamat.2013.07.039.

[46] L.M. Felix, C.C.F. Kwan, N.Y. Zhou, The effect of pulse energy on the defects and microstructure of electro-spark-Deposited inconel 718, Metall. Mater. Trans. A 50 (2019) 4223–4231, https://doi.org/10.1007/s11661-019-05332-8.

[47] S. Singh, Y. Guo, B. Winiarski, T.L. Burnett, P.J. Withers, M. De Graef, High resolution low kV EBSD of heavily deformed and nanocrystalline Aluminium by dictionary-based indexing, Sci. Rep. 8 (2018) 1–8, https://doi.org/10.1038/s41598-018-29315-8.

[48] S. Kuroda, T.W. Clyne, The quenching stress in thermally sprayed coatings, Thin Solid Films 200 (1991) 49–66, https://doi.org/10.1016/0040-6090(91)90029-W.

[49] A.J. Wilkinson, D.J. Dingley, Quantitative deformation studies using electron back scatter patterns, Acta Metall. Mater. 39 (1991) 3047–3055, https://doi.org/10.1016/0956-7151(91)90037-2.

[50] A. Oradei-Basile, J.F. Radavich, A current T-T-T diagram for wroughtalloy 718, Superalloys 718, TMS, 1991, pp. 325–335, https://doi.org/10.7449/1991/Superalloys_1991_325_335 625 Var. Deriv.

[51] J.-C. Zhao, M. Larsen, V. Ravikumar, Phase precipitation and time–temperature-transformation diagram of Hastelloy X, Mater. Sci. Eng. A 293 (2000) 112–119, https://doi.org/10.1016/S0921-5093(00)01049-2.

[52] H.M. Tawancy, Long-term ageing characteristics of Hastelloy alloy X, J. Mater. Sci. 18 (1983) 2976–2986, https://doi.org/10.1007/BF00700780.

[53] Q. Han, R. Mertens, M.L. Montero-Sistiaga, S. Yang, R. Setchi, K. Vanmeensel, B. Van Hooreweder, S.L. Evans, H. Fan, Laser powder bed fusion of Hastelloy X: effects of hot isostatic pressing and the hot cracking mechanism, Mater. Sci. Eng. A 732 (2018) 228–239, https://doi.org/10.1016/j.msea.2018.07.008.

[54] M. Suraratchai, J. Limido, C. Mabru, R. Chieragatti, Modelling the influence of machined surface roughness on the fatigue life of aluminium alloy, Int. J. Fatigue 30 (2008) 2119–2126, https://doi.org/10.1016/j.ijfatigue.2008.06.003.

[55] D. Arola, C.L. Williams, Estimating the fatigue stress concentration factor of machined surfaces, Int. J. Fatigue 24 (2002) 923–930, https://doi.org/10.1016/S0142-1123(02)00012-9.
[56] J.W. Pegues, N. Shamsaei, M.D. Roach, R.S. Williamson, Fatigue life estimation of additive manufactured parts in the as-built surface condition, Mater. Des. Process. Commun. 1 (2019) e36, https://doi.org/10.1002/mdp2.36.
[57] M.A.S. Torres, H.J.C. Voorwald, An evaluation of shot peening, residual stress and stress relaxation on the fatigue life of AISI 4340 steel, Int. J. Fatigue 24 (2002) 877–886, https://doi.org/10.1016/S0142-1123(01)00205-5.
[58] D. Gopikrishna, S.N. Jha, L.N. Dash, Influence of microstructure on fatigueproperties of alloy 718, Superalloys 718, TMS, Pittsburgh, Pennsylvania, 1997, pp. 567–573, https://doi.org/10.7449/1997/Superalloys_1997_567_573 625, 706 Var. Deriv..
[59] A.D. Boyd-Lee, Fatigue crack growth resistant microstructures in polycrystalline Ni-base superalloys for aeroengines, Int. J. Fatigue 21 (1999) 393–405, https://doi.org/10.1016/S0142-1123(98)00087-5.
[60] S. Leuders, M. Thöne, A. Riemer, T. Niendorf, T. Tröster, H.A. Richard, H.J. Maier, On the mechanical behaviour of titanium alloy TiAl6V4 manufactured by selective laser melting: fatigue resistance and crack growth performance, Int. J. Fatigue 48 (2013) 300–307, https://doi.org/10.1016/j.ijfatigue.2012.11.011.
[61] J.J. Schirra, R.H. Caless, R.W. Hatala, The effect of lavesphase on the mechanicalproperties of wrought and cast + HIP inconel 718, Superalloys 718, TMS, 1991, pp. 375–388, https://doi.org/10.7449/1991/Superalloys_1991_375_388 625 Var. Deriv..
[62] S. Sui, J. Chen, E. Fan, H. Yang, X. Lin, W. Huang, The influence of Laves phases on the high-cycle fatigue behavior of laser additive manufactured Inconel 718, Mater. Sci. Eng. A 695 (2017) 6–13, https://doi.org/10.1016/j.msea.2017.03.098.